Biomaterials Translational

Four-dimensional-printed personalized shape memory NiTi implant for minimally invasive delivery in cavitary bone defect reconstruction

Zhuangzhuang Li[1,2#], Minxun Lu[1,2#], Shanfang Zou[3], Ruicheng Liu[3], Haoyuan Lei[4], Yitian Wang[1,2], Yuqi Zhang[1,2], Yong Zhou[1,2], Changchun Zhou[4], Yi Luo[1,2*], Li Min[1,2*], and Chongqi Tu[1,2*]

ABSTRACT

Integrating 4D printing technology in medical implants offers promising advancements for minimally invasive delivery (MID) and personalized orthopedic solutions. This study presents a 4D-printed shape memory nickel-titanium (NiTi) mesh implant for cavitary bone defect reconstruction, enabling a time-dependent shape transformation. Fabricated through selective laser melting (80 W laser power, 600 mm/s scanning speed, 70 μm hatch spacing, 25 μm layer thickness), the implant can be compressed during implantation and recover its original shape. Micro-computed tomography analysis confirmed high geometric fidelity (D50 = 58 μm), while scanning electron microscopy-energy dispersive spectroscopy analysis revealed a uniform microstructure and confirmed the homogeneous distribution of Ni/Ti across the mesh implant. Phase transformation testing showed that the austenite finish temperatures (austenite finish) of the as-built sample and the acid-washed sample were below the 37°C physiological threshold. Compression testing indicated that a force of 156 N was required for 30% deformation, with complete recovery to its pre-defined shape. Clinically, the implant reduced cortical bone fenestration by 20%. Post-operative imaging at 6 and 12 months showed excellent osseointegration and minimal residual cavities. Functional assessments at 12 months indicated excellent recovery, with a Musculoskeletal Tumor Society score of 29. In the present study, the clinical use of the 4D-printed mesh implant demonstrated not only satisfactory osteointegration but also a practical advantage in surgical handling. The shape recovery of the implant from a compressed state to its pre-designed shape allowed for MID and precise fit to the defect contour.

Keywords:
4D printing; Shape memory effect; Nickel–titanium alloy; Selective laser melting; Minimally invasive surgery; Orthopedic implants

#Authors contributed equally.

***Corresponding authors:**
Yi Luo,
orthop_luoyi@scu.edu.cn;
Li Min,
minli1204@scu.edu.cn;
Chongqi Tu,
tucq@scu.edu.cn

How to cite this article:
Li Z, Lu M, Zou S, *et al.* Four-dimensional-printed personalized shape memory NiTi implant for minimally invasive delivery in cavitary bone defect reconstruction. *Biomater Transl.* 2026, 7(1), 144-154.

doi: 10.12336/bmt.25.00009

1. Introduction

Cavitary bone defects are often associated with benign tumors and typically occur in the metaphyseal region.[1] These defects frequently leave the surrounding cortical bone intact but present significant challenges for bone repair due to their irregular geometry and structural damage. Traditional reconstruction methods, including autografts, allografts, and cement filling, frequently encounter limitations, such as limited mechanical support and poor osteointegration.[2] In recent years, 3D printing has enabled the rapid and cost-effective fabrication of anatomically customized implants.[3,4] Previous research demonstrated the effectiveness and advantages of personalized 3D-printed titanium mesh implants combined with autologous bone grafting in cavitary bone defect reconstruction, including mechanical support and improved surgical outcomes.[5] However, their implantation required large cortical bone fenestrations, resulting in unnecessary loss of cortical bone. Despite advances in minimally invasive orthopedic techniques,[6] Such as percutaneous bone grafting and injectable cement, reliable minimally invasive

delivery (MID) methods for structural-support implants remain limited. The advent of 4D printing technology has emerged as an advancement in biomedical engineering.[7,8] This technology extends 3D printing by incorporating smart materials with shape memory properties, enabling the production of dynamic implants. Utilizing the shape memory effect (SME), 4D-printed devices can undergo programmed transformations when triggered by external stimuli, such as temperature, light, and pH.[9,10] This unique adaptability makes 4D-printed implants effective for MID, where they can reshape or self-assemble after implantation. However, material selection remains critical for load-bearing applications. While shape memory polymers[9,11] and hydrogels[12,13] have been explored, their limitations (low mechanical strength and structural fragility) hinder clinical translation. Nickel–titanium (NiTi) alloys stand out due to their remarkable mechanical performance and functional properties.[14,15] In addition, recognized as one of the metallic biomaterials approved by the United States (US) Food and Drug Administration for medical applications, NiTi alloys have been widely employed in bone fixation systems.[16,17] Their exceptional biocompatibility ensures minimal adverse reactions, while their corrosion resistance and mechanical durability make them ideal for orthopedic implants.

The growing exploration of NiTi alloys for 4D printing applications has propelled breakthroughs in metal additive manufacturing, particularly through the selective laser melting (SLM) method.[18,19] SLM allows the precise fabrication of complex NiTi geometries while offering meticulous control over microstructure and functional properties. Recent progress in this field has focused on optimizing SLM process parameters, such as laser power, scanning speed, and hatch spacing, to produce NiTi structures tailored for biomedical use.[20-22] Specifically, in our previous research, the critical ability to adjust the phase transformation temperature of NiTi alloys in line with body temperature (BT) was achieved.[23] These developments have not only overcome a major barrier in biomedical applications but also paved the path for the fabrication of adaptive, patient-specific implants suitable for MID.

This study aims to introduce a novel 4D-printed NiTi mesh implant specifically designed for the reconstruction of cavitary bone defects. The implant's properties, shape recovery performance, and clinical feasibility in orthopedic surgery are evaluated. By integrating experimental characterization with computational modeling, this study seeks to establish a framework for the application of 4D-printed orthopedic implants.

2. Materials and methods

2.1. Implant design

A 25-year-old female presented with left knee swelling and pain. Imaging findings revealed a lesion in the distal femur, and the details are provided in Figure S1. A biopsy confirmed the diagnosis of osteoblastoma. After obtaining informed consent, implant design and surgical planning were initiated. The design of the patient-specific implant began with the acquisition of the patient's anatomical data through high-resolution computed tomography (CT) imaging (**Figure 1A**). Data were exported in Digital Imaging and Communications in Medicine (DICOM) format and imported into Mimics software (Version 24.0; Materialize, Belgium) for 3D reconstruction. Using Mimics, the defect's contour was extracted. The reconstructed model was then exported into Geomagic Studio (Version 2019; 3D Systems, US) for smoothing and refinement, eliminating irregularities in the contour surface. The implant model, based on the defect contour, was divided into two main components: The padding component and the deformation component. The padding component was designed to provide stable support and sufficient filling of the defect, while the deformation component allows deformation during implantation and recovery to its pre-defined shape at BT. The padding and deformation components were assembled through curvature-based fitting. The model was further processed using Meshmax software (Version 2.1, Scanco Medical, Switzerland) to generate a surface mesh (thickness of 0.5 mm) for both components (**Figure 1B**). To enhance functionality, bone grafting windows were strategically added to the porous mesh structure. These windows were designed to facilitate the insertion of autologous iliac-cancellous bone grafts, supporting bone regeneration and integration with the host tissue. Once finalized, the design file was saved in stereolithography (STL) format, preparing it for fabrication using SLM technology.

2.2. Materials and fabrication

The fabrication process utilized an SLM system (Mlab, Concept Laser, Germany), operated under an inert argon atmosphere to minimize oxidation (**Figure 1C**). In detail, Ni-rich powder (55.68 wt.% Ni) was used for the fabrication of the implant. The SLM parameters – laser power (80 W), scanning speed (600 mm/s), hatch spacing (70 μm), and layer thickness (25 μm) – were rigorously selected in our prior study,[23] where shape recovery rate and tensile strength served as the primary optimization targets. These parameters corresponded to an energy density of 65.3 J/mm^3 according to Equation I:

$$E = \frac{P}{v \times h \times t} \quad \text{(I)}$$

where E represents the energy density (J/mm^3), P is the laser power (W), v is the scanning speed (mm/s), h is the hatch spacing (μm), and t is the layer thickness (μm). A ± 45° alternating laser scanning pattern was employed for consecutive layers, promoting a uniform microstructure and effectively reducing residual stress. Post-fabrication, the implant model underwent acid wash (10% HF, 40% HNO_3, and 50% H_2O) for 3 min to remove residual powder particles.

[1]Department of Orthopedics, Orthopedic Research Institute, West China Hospital, Sichuan University, Chengdu, Sichuan, China; [2]Model Worker and Craftsman Talent Innovation Workshop of Sichuan Province, Chengdu, Sichuan, China; [3]Tianqi Additive Manufacturing Co., Ltd, Chengdu, Sichuan, China; [4]National Engineering Research Centre for Biomaterials, Sichuan University, Chengdu, Sichuan, China

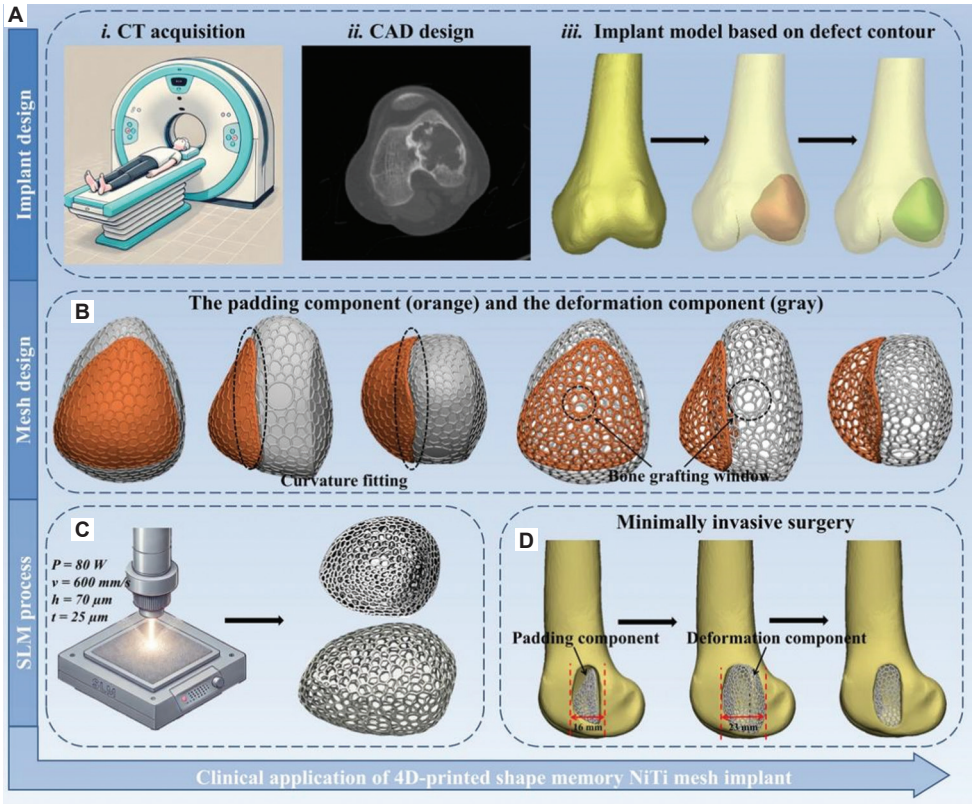

Figure 1. Workflow for the design, fabrication, and clinical application of a patient-specific 4D-printed shape memory NiTi mesh implant. (A) Computed tomography imaging was used to acquire anatomical data, followed by defect reconstruction and implant modeling with Mimics and Geomagic Studio to create a design tailored to the defect contour. (B) The implant comprises two components: A padding component (orange) for defect support and a deformation component (gray) with shape memory properties for minimally invasive implantation. (C) The implant was fabricated using SLM with parameters: Laser power of 80 W, scanning speed of 600 mm/s, hatch spacing of 70 μm, and layer thickness of 25 μm. (D) In the clinical application, the implant is positioned in the defect site, with the padding component providing structural support and the deformation component recovering its shape at body temperature.
Abbreviation: CAD: Computer-aided design.

2.3. Implant characterization

Due to the deformation component as the core of the MID, the subsequent characterization and testing focused on the deformation component, which was also referred to as the mesh implant in the following sections of the paper. The mesh implant was first evaluated using a GE Nanotom micro-CT (General Electric, US) system, operating at a tube voltage of 140 kV, current of 100 μA, and exposure time of 1000 ms. The reconstructed 3D model was generated in VGStudio MAX (Version 3.1; Volume Graphics, Germany). To determine printing accuracy, surface deviation analysis was performed by comparing the reconstructed model to the original design by computer-aided design (CAD) software. The analysis produced 3D color maps, and the median deviation value (D_{50}) was calculated to quantify discrepancies between the fabricated and designed geometry.

To further characterize the surface morphology of the mesh implant, scanning electron microscopy (SEM) was performed using the Zeiss EVO 10 SEM (Carl Zeiss AG, Germany). A mesh region with a diameter of approximately 1 cm was selected for detailed analysis. In addition, elemental mapping was conducted to analyze the distribution of key elements (Ni and Ti) across the selected region.

The phase transformation behavior of the mesh implant was analyzed using a differential scanning calorimeter (DSC; NETZSCH DSC 204, NETZSCH, Germany). The analysis was performed at a controlled cooling/heating rate of 10°C/min over a temperature range of −100°C – 100°C. The transformation temperatures were determined using the intersection point method, which identifies the intersection between two tangent lines on the DSC curve. Key transformation temperatures, including martensite start (M_s), martensite peak (M_p), and martensite finish (M_f), as well as austenite start (A_s), austenite peak (A_p), and austenite finish (A_f), were recorded.

2.4. Shape memory testing

The shape memory behavior of the mesh implant was evaluated through controlled deformation and subsequent recovery testing. After undergoing liquid nitrogen cooling, the deformation component experienced a compression of 7 mm from its initial height, primarily through controlled bending deformation of the mesh structure. The deformation component underwent an engineering strain (ε) of 30%, as calculated using Equation II:

$$\varepsilon = \frac{\Delta L}{L_0} \quad \text{(II)}$$

where ε represents the engineering strain, ΔL is the change in length of the implant (7 mm), and L_0 is the original length of the implant (23 mm). Following deformation, the component was immersed in 37°C warm water to simulate BT, activating the SME and enabling it to recover to its pre-defined shape.

To analyze the mechanical properties of the deformation component during compression, a uniaxial compression test was conducted at a displacement rate of 0.2 mm/min using an Instron 5982 universal testing machine (Instron, US). The digital image correlation (DIC) technique was utilized during the test to capture real-time stress distribution and strain patterns across the component.

2.5. Clinical application

The surgery was performed at West China Hospital after obtaining the patient's signed informed consent and ethical approval from the hospital's Institutional Review Board. In detail, under general anesthesia, the patient was positioned supine on an operating table. A skin incision was made along the lateral aspect of the targeted site, and subcutaneous tissues were carefully dissected. The musculature overlying the cortical bone was retracted to provide a clear view of the surgical field. A cortical bone window was created using a microdrill and bone chisel, precisely sized and shaped based on pre-operative planning. Tumor or necrotic tissue was meticulously removed using curettes and high-speed drills. Alcohol irrigation and ablation using a high-frequency electrotome (GD350 Series, Hooton Electronics Co., Ltd., China) were applied to reduce the risk of recurrence. Then, autologous cancellous bone grafts were harvested from the iliac crest and crushed into smaller fragments to facilitate packing. The padding component was filled with the crushed cancellous bone grafts and carefully implanted into the prepared defect through cortical fenestration (**Figure 1D**). The deformation component was compressed in a liquid nitrogen bath to achieve the desired deformation and maintained in ice water to preserve its compressed state. The transverse diameter of the deformation component was reduced by 30%. Subsequently, the compressed deformation component was introduced through the bone window. Once in place, the deformation component expanded to its pre-defined shape at BT. An additional autologous iliac bone graft was then placed into the structure of the deformation component to promote osseointegration.

2.6. Post-operative follow-up

Follow-up visits were conducted at 1 month, 3 months, 6 months, and annually thereafter. At each follow-up, X-ray scans were conducted to monitor the placement and stability of the implant. In addition, tomosynthesis-Shimadzu metal artifact reduction technology (T-SMART) was utilized to evaluate osseointegration. At the final follow-up, a high-resolution 3D CT scan was conducted. The imaging data were processed using VGStudio MAX software to reconstruct the cavitary defect region. Quantitative measurement was performed to assess the effectiveness of the reconstruction, including calculating the residual cavity volume. The functional recovery of the patient was assessed using the Musculoskeletal Tumor Society (MSTS) score.[24] The assessment included pain, limb function, emotional acceptance, walking ability, and the use of walking aids.

3. Results

3.1. Printability assessment

The structural integrity and fabrication accuracy of the 4D-printed NiTi mesh implant were evaluated using micro-CT. **Figure 2A** presents the reconstructed model in the coronal, transverse, and sagittal views. These images confirmed the successful reproduction of the CAD model design with high geometric fidelity. Deviation analysis, as shown in **Figure 2B**, quantified the dimensional discrepancies between the fabricated implant and the original CAD model. The calculated D_{50} was 58 μm (**Figure 2C**), indicating a high level of precision achieved through the SLM process. The results collectively demonstrated that the SLM process employed in this study ensures excellent printability and precise structural reproduction of the NiTi mesh implant.

3.2. Morphology

The SEM images (**Figure 2D** and **G**) revealed the surface morphology of the as-built and acid-washed NiTi mesh structures. In the as-built sample, residual powder particles were observed adhering predominantly around the struts. After acid washing, the surface became significantly smoother, with minimal powder adhesion, indicating that the acid treatment effectively removed the residual particles and improved the surface quality. In addition, no significant defects were observed on the surface, such as cracks or irregular defects. The energy dispersive spectroscopy (EDS) elemental mapping (**Figure 2E** and **H**) demonstrated a homogeneous distribution of Ni and Ti across the mesh structure in both the as-built and acid-washed samples. The mapping also confirmed the minimal presence of carbon (C), oxygen (O), and nitrogen (N), likely attributed to minor surface oxidation or environmental exposure during sample preparation. The EDS spectra revealed strong peaks corresponding to Ni and Ti, consistent with the NiTi alloy composition (**Figure 2F** and **I**). These findings indicate that the SLM fabrication method produced high-quality NiTi structures with uniform elemental distribution. The post-processing acid-washing step further improved surface morphology.

3.3. Phase transformation behavior

The phase transformation behavior of the NiTi mesh implant was evaluated using DSC, and the corresponding DSC curves are presented in **Figure 3A**. Both the as-built and acid-washed samples exhibited distinct thermal peaks corresponding to the martensite and austenite phase transformations. The A_f temperatures of the as-built sample and the acid-washed sample were both below the physiological threshold of 37°C (**Table 1**). These results confirmed that the SME can be activated at BT, making the implants highly suitable for clinical use.

3.4. SME of deformation component

The shape memory behavior of the deformation component was evaluated through compression and recovery tests. **Figure 3B** illustrates the shape recovery process, demonstrating

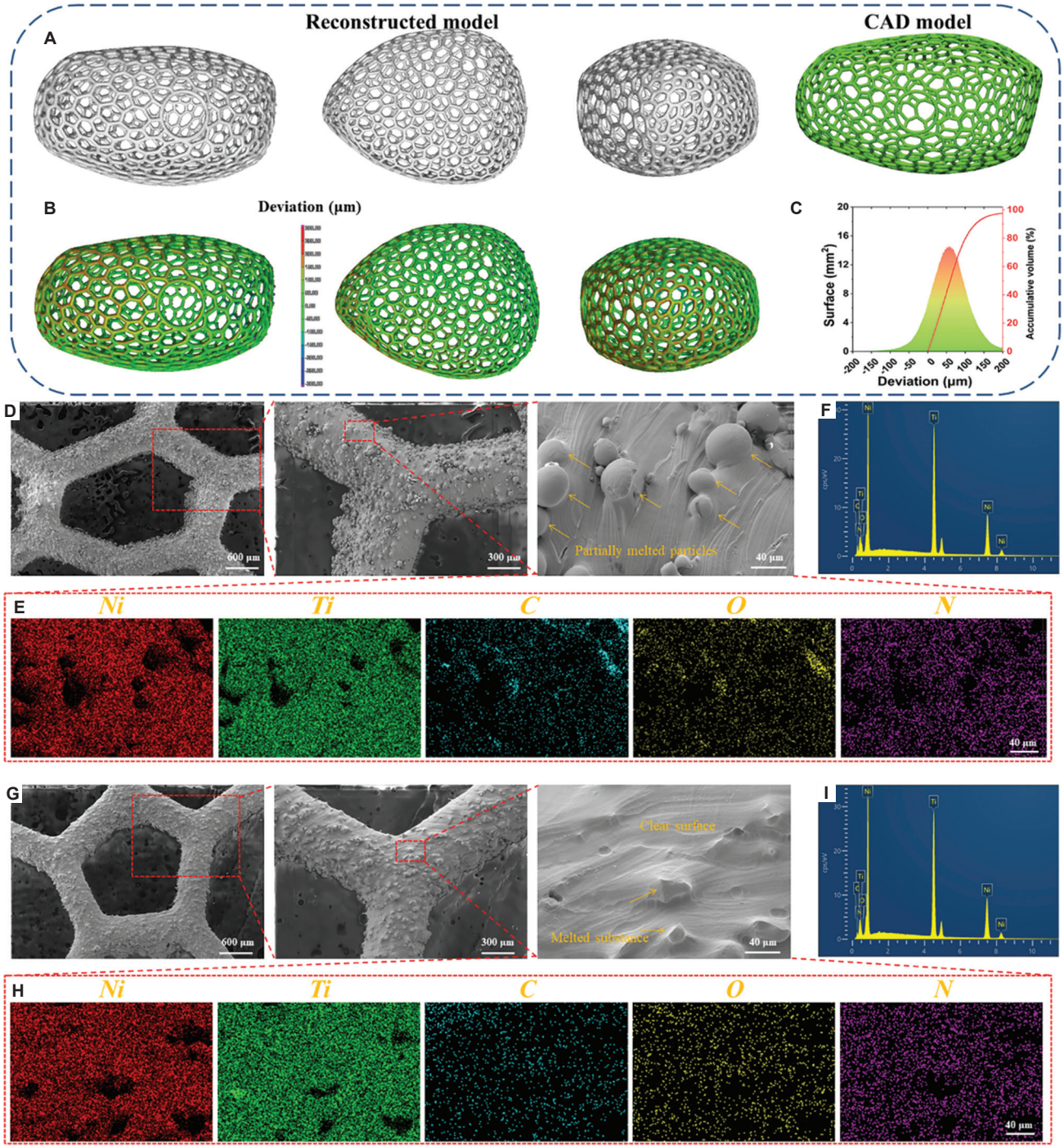

Figure 2. Characterization of the NiTi mesh implant. (A) Reconstructed model in coronal, transverse, and sagittal views, showing high geometric fidelity compare with the design of the computer-aided design (CAD) software. (B) Deviation analysis visualizes dimensional discrepancies between the fabricated implant and the original CAD model. (C) Distribution of deviation values, with the median deviation (D50) of 58 μm, confirming the precision of the selective laser melting process. (D) Scanning electron microscopy (SEM) images of the as-built NiTi mesh structure, showing residual powder particles predominantly adhering to the struts (scale bar: 600 μm, magnification power: 60×). (E) Energy dispersive spectroscopy (EDS) elemental mapping of the as-built sample, indicating a uniform distribution of Ni and Ti, with minimal presence of C, O, and N (scale bar: 40 μm, magnification power: 1000×. (F) EDS spectra of the as-built sample, revealing strong peaks for Ni and Ti, consistent with the NiTi alloy composition. (G) SEM images of the acid-washed NiTi mesh structure, showing a significantly smoother surface with minimal powder adhesion (scale bar: 600 μm, magnification power: 60×). (H) EDS elemental mapping of the acid-washed sample, demonstrating uniform Ni and Ti distribution with minimal traces of C, O, and N (scale bar: 40 μm, magnification power: 1000×). (I) EDS spectra of the acid-washed sample, confirming strong peaks for Ni and Ti.

that the deformation component completely restored its pre-defined geometry upon immersion in 37°C water after being compressed by 30% of its original height at liquid nitrogen cooling. Further analysis was conducted to evaluate the

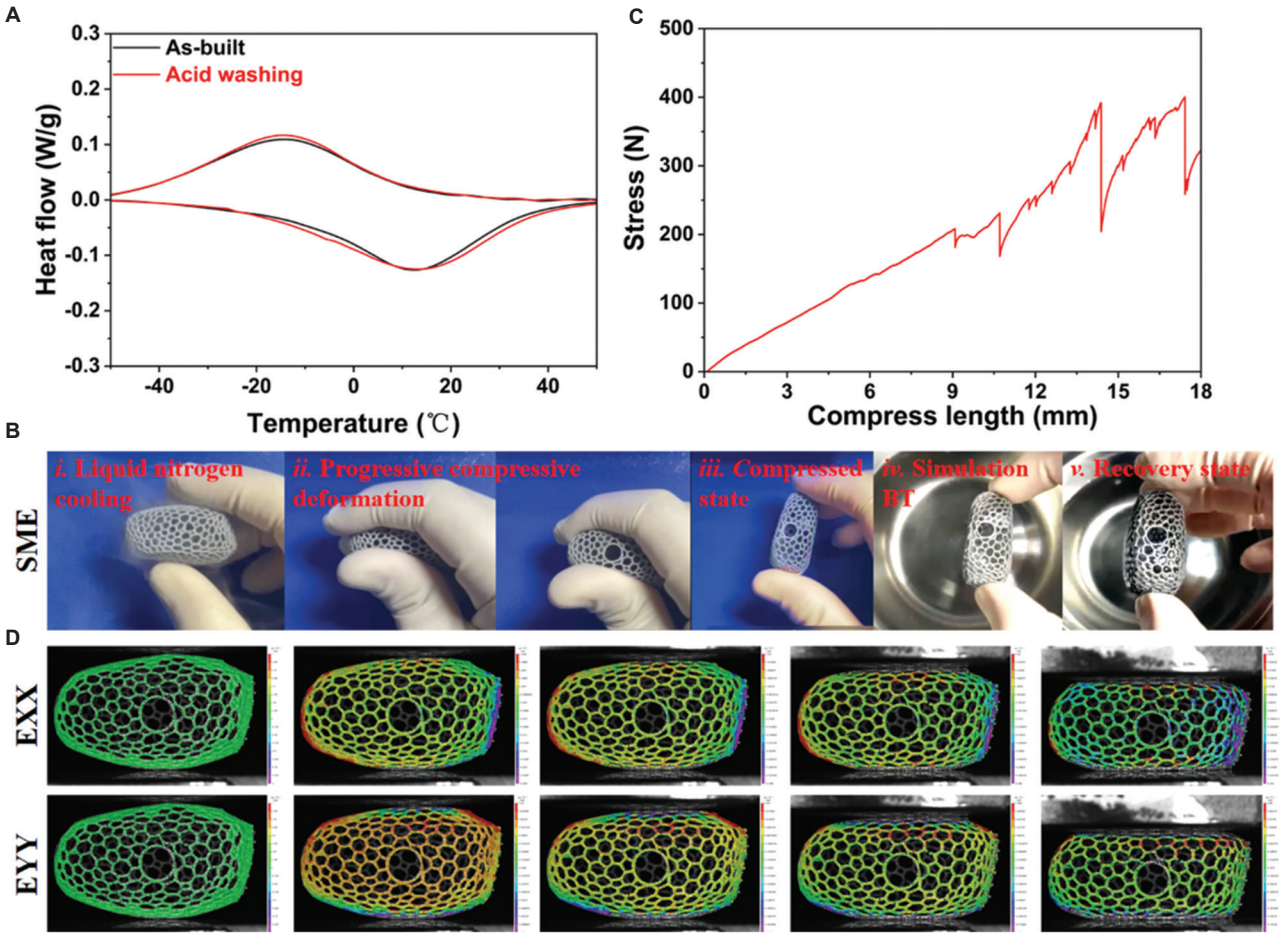

Figure 3. Shape memory effect and mechanical properties of the NiTi mesh implant. (A) DSC curves of the as-built and acid-washed samples. The A_f temperatures for both samples are below 37°C, confirming that the SME can be activated at body temperature. (B) Sequential images of the shape recovery process of the deformation component: (i) Liquid nitrogen cooling, (ii) compression, (iii) retention of compressed state, (iv) activation at 37°C water immersion, and (v) recovery to its pre-defined geometry. (C) Stress–strain curve from the compression test, showing that 156 N force is required to achieve 7 mm compression. (D) DIC strain distribution maps during compression, illustrating deformation characteristics of the mesh structure. EXX maps indicate lateral expansion in the X direction, while EYY maps demonstrate a generally uniform vertical strain distribution with minor upward strain in bending regions, highlighting the uniform load distribution without significant stress concentrations.
Abbreviations: Af: Austenite finish; DSC: Differential scanning calorimetry; ; DIC: Digital image correlation; SME: Shape memory effect.

Table 1. Key transformation temperatures of the as-built and acid-washed samples

Sample	M_s (℃)	M_p (℃)	M_f (℃)	A_s (℃)	A_p (℃)	A_f (℃)
As-built	11	−14	−37	−10	12	36
Acid-washed	10	−14	−39	−15	13	36

Notes: M_s, M_p, and M_f: Martensite transformation start, peak, and finish temperature, respectively; A_s, A_p, and A_f: Austenite transformation start, peak, and finish temperature, respectively

mechanical response during deformation. The stress-strain curve obtained from the compression test (**Figure 3C**) revealed that a force of 156 N was required to achieve 30% compression (7 mm).

The DIC analysis provided detailed strain distribution maps (EXX and EYY), which highlighted the deformation characteristics of the mesh structure during compression (**Figure 3D**). The EXX map represents the normal strain in the X direction, indicating the deformation of the material along the horizontal axis. Similarly, the EYY map represents the normal strain in the Y direction, corresponding to the deformation along the vertical axis. In detail, the EXX map revealed a slight lateral expansion of the structure under compression. The EYY map demonstrated a generally uniform strain distribution. However, due to the predominantly bending nature of the deformation, minor upward strains were observed in the small bending regions. These strain maps highlighted the uniform load distribution across the mesh structure, with no significant stress concentrations.

3.5. Clinical outcomes

The clinical application of the 4D-printed NiTi mesh implant demonstrated favorable outcomes. **Figure 4A-F** presents intraoperative images, highlighting a reduced size in the cortical bone fenestration. While the planned reduction in the transverse diameter of the bone window was 30%, the actual reduction achieved was 20% due to minor over-removal during tumor curettage. The adaptive design of the implant eliminated the need for extensive defect site modifications, resulting in

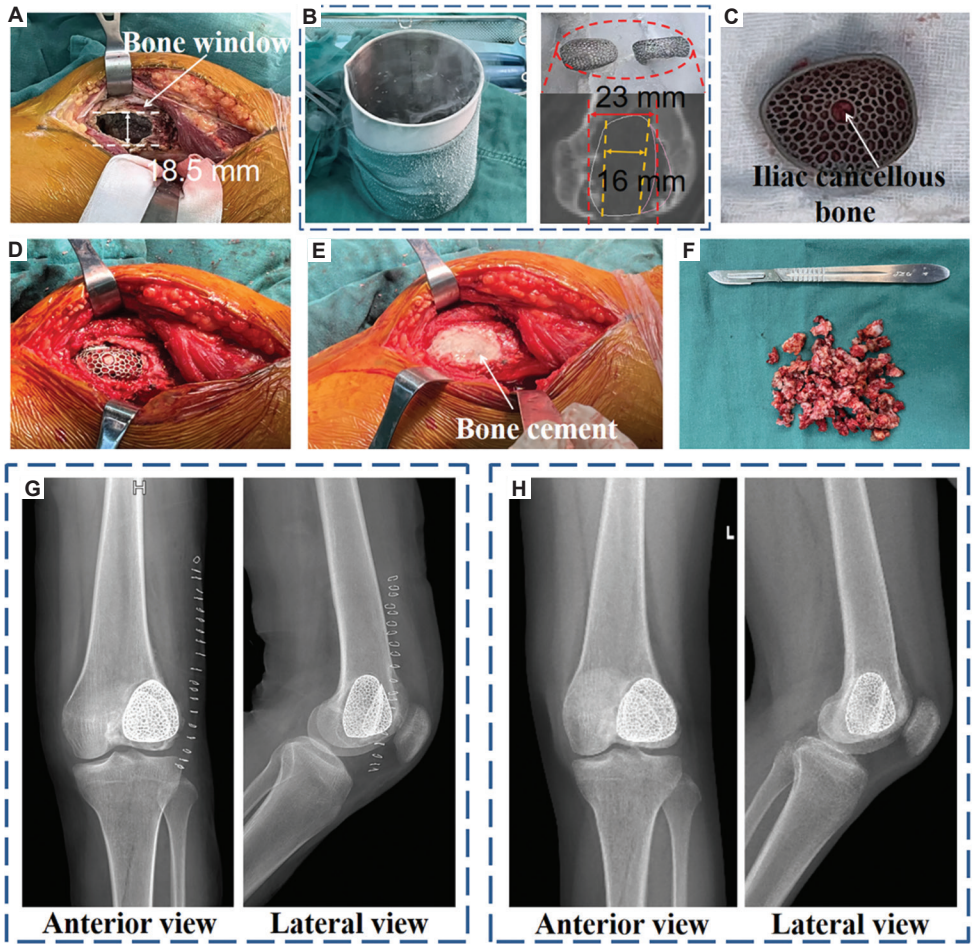

Figure 4. Surgical procedure and post-operative evaluation of the NiTi implant. (A) Intraoperative placement of the NiTi implant, showing a reduced size in cortical bone fenestration. (B) Preparation of the implant in liquid nitrogen for compressive deformation. (C) Iliac-cancellous bone graft harvested for filling the mesh structure form bone grafting window. (D and E) Placement of the NiTi implant into the defect and subsequent bone cement closure. (F) A specimen of curetted bone tissue obtained during the procedure. (G and H) X-ray images at post-operative 1 month (G) and 6 months (H) show stable implant positioning without signs of loosening or mechanical failure.

a shorter surgical time of 149 min and intraoperative blood loss of 200 mL. X-ray imaging at post-operative 1 month (**Figure 4G**) and 6 months (**Figure 4H**) demonstrated proper implant placement within the cavitary bone defect.

The T-SMART images at post-operative 1 month (**Figure 5A**) and 6 months (**Figure 5B**) demonstrate artifact-reduced, high-resolution views of the bone-implant interface. At 6 months, there was evidence of increased bone remodeling and consolidation compared to the 1-month follow-up. At the 12-month follow-up, high-resolution 3D-CT imaging was utilized to assess the long-term effectiveness of the implant reconstruction. Quantitative analysis revealed the presence of a few residual cavities, as shown in the reconstructed 3D models (**Figure 5C-G**). The volume of the residual cavities was calculated, with all cavities measuring <50 mm^3 (**Figure 5H**). The total residual cavity volume accounted for <1% of the analyzed region. This indicates excellent osseointegration and a highly effective reconstruction with minimal voids remaining.

At the 12-month follow-up, functional assessments revealed excellent recovery. The patient exhibited satisfactory knee function, sufficient for daily activities, as evaluated by an MSTS score of 29. During the post-operative follow-up, no implant-related complications, such as infection, aseptic loosening, and mechanical failure, were observed. In addition, no signs of systemic inflammation, allergic reactions, or organ dysfunction were observed. Blood routine and biochemical parameters remained within normal ranges post-operatively, and no adverse effects were reported.

4. Discussion

This study demonstrates the development and successful application of a 4D-printed shape memory NiTi mesh implant for cavitary bone defect reconstruction. The integration of patient-specific design and SME addresses the limitations of traditional reconstruction methods. Compared to static 3D-printed implants, the 4D-printed NiTi mesh implant allows for MID, preserving more cortical bone. Furthermore, the SME facilitates shape recovery at physiological temperature, improving the fit within irregular defect geometries. These advancements not only provide a viable solution for cavitary bone defect reconstruction but also highlight the broader potential of 4D printing technology in personalized orthopedic applications.

SLM has emerged as a research hotspot for fabricating NiTi alloys, primarily due to its exceptional precision and capability

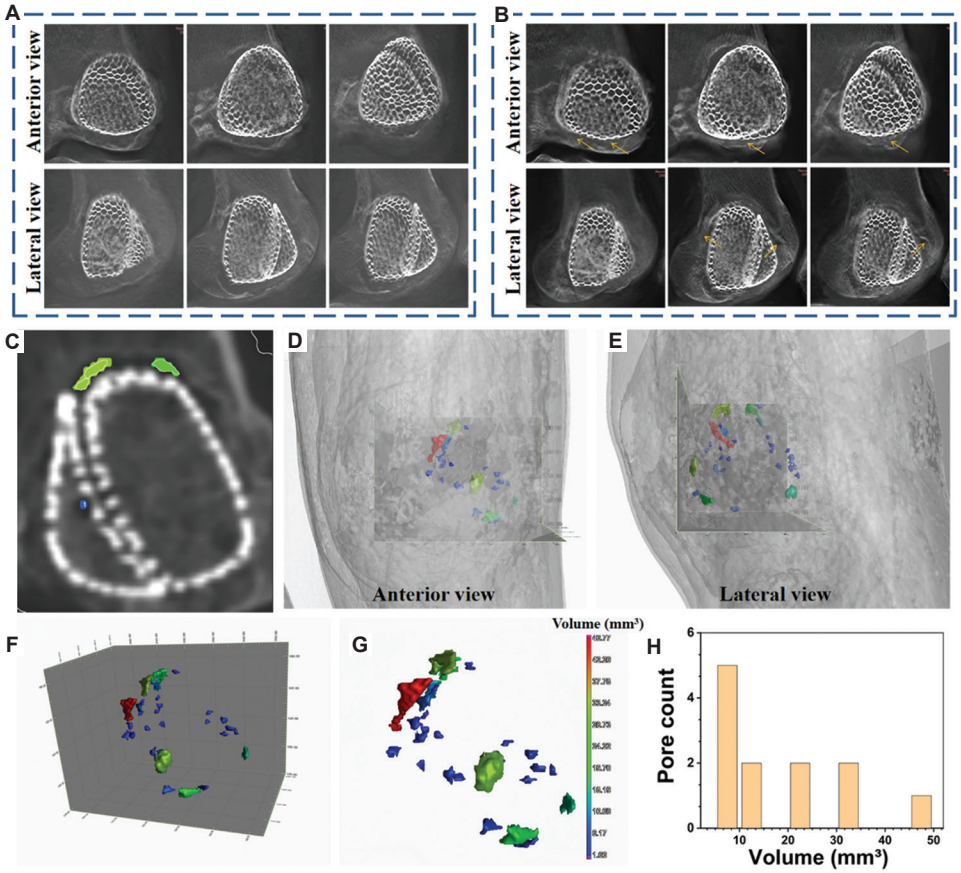

Figure 5. Post-operative imaging and analysis of bone remodeling around the NiTi implant. (A and B) Tomosynthesis-Shimadzu metal Artifact reduction technology images at post-operative 1 month and 6 months demonstrate increased bone remodeling and consolidation. (C) The 3D-computed tomography cross-sectional view at 12 months shows minor residual cavities near the implant. (D and E) Reconstructed anterior and lateral views of residual cavities in the implant region. (F and G) A 3D representation of residual cavity distribution and volumes, indicating minimal residual voids. (H) Quantitative analysis of cavity volumes, with all measured cavities <50 mm^3, and the total volume accounting for <1% of the analyzed region.

for free-form fabrication of complex geometries.[20,25] This technology can produce intricate designs, which are challenging to achieve with traditional manufacturing methods. In this study, the fabrication of porous structures was successfully achieved, showcasing SLM's effectiveness in creating complex implant designs. The accuracy of the SLM process was quantitatively evaluated through deviation analysis, with a D_{50} value of 58 μm, demonstrating the high fidelity of the printed implant. Compared with previous studies, which reported deviation ranges of 25 – 150 μm,[26-28] our results demonstrate a comparable level of dimensional accuracy. This precision is particularly significant for personalized implants to accurately match individual anatomical requirements. After fabrication, the surface of the as-built NiTi samples commonly exhibited adhered powder particles, a phenomenon referred to as "powder adhesion."[29,30] These adhered particles can pose several potential issues, including the risk of detachment during use, which may create debris that could negatively impact surrounding tissues or compromise implant performance. Moreover, these particles can hinder cellular integration by creating an uneven surface topography and potentially exposing particles that could impede cellular attachment and growth.[31] To address these concerns, an acid-washing treatment was employed in this study. Post-treatment surface morphology analysis revealed a significant reduction in adhered particles, resulting in a cleaner surface. Elemental analysis confirmed that the primary elemental composition remained unchanged; indicating that the acid washes effectively removed surface contaminants without adversely affecting the material's chemical integrity.

The phase transformation temperature plays a critical role in determining the SME of NiTi alloys.[32] For implants designed to operate within the human body, the A_f temperature should remain below 37°C to ensure proper activation of the SME under physiological conditions. In this study, both the as-built and acid-washed NiTi samples exhibited A_f temperatures below 37°C, indicating their strong potential for biomedical applications. Previous studies have shown that the phase transformation temperatures of NiTi alloys depend heavily on the SLM process parameters.[33,34] For instance, higher energy densities tend to increase the phase transformation temperature, potentially due to greater evaporation of Ni, which alters the Ni–Ti ratio and affects the material's phase transformation behavior.[35] The process parameters employed in this study, including a laser power of 80 W, scanning speed of 600 mm/s, and hatch spacing of 70 μm, were carefully optimized. Interestingly, the phase temperatures of

the acid-washed sample were nearly identical to those of the as-built sample. This can be attributed to the fact that the as-built sample was polished before testing to remove surface powder particles. As a result, the transformation temperatures primarily reflect the intrinsic properties of the bulk material rather than surface modifications. The acid wash, primarily aimed at improving surface cleanliness by removing adhered powder particles, targeted only the surface layer and did not affect the core microstructure or elemental composition. Consequently, the phase transformation characteristics, which reflect the properties of the internal matrix, remained similar.

The SME of the fabricated NiTi mesh implant was evaluated through *in vitro* compression testing. In this study, the implant demonstrated full recovery after being compressed 30%, showcasing its excellent shape memory capabilities. Previous research has widely reported that shape recovery rates are closely associated with the level of applied strain, with complete recovery typically observed at strain levels up to 8 – 10%.[36,37] The strain applied in this study was calculated as engineering strain based on the travel distance of the implant. Notably, the strain in the porous structure corresponds to bending deformation, meaning the actual strain experienced by the material is significantly smaller than the engineering strain calculated from the overall compression. This explains the implant's ability to achieve complete recovery under the tested conditions. The study further explored the mechanical performance during the deformation process using a universal testing machine, determining the force required to achieve 30% compression. Interestingly, the measured force appeared higher than the manual compression experience. This discrepancy can be attributed to differences in the compression mechanisms. In mechanical testing, the entire perimeter of the implant was compressed uniformly, requiring greater force. In contrast, manual compression involved stepwise deformation, where smaller areas were compressed sequentially, reducing the required force for the same strain. This phenomenon aligns with the principle that smaller contact areas experience lower forces under identical strain conditions, allowing manual compression to be performed with relative ease. Strain distribution during the deformation process was analyzed using DIC. In the strain maps represented by EXX and EYY, the strain distribution was generally uniform across most regions of the mesh structure.

The clinical application of the 4D shape memory NiTi mesh implant yielded promising outcomes. The surgical time was reduced due to the implant's ability to conform precisely to the defect shape without requiring extensive modification of the defect site. This eliminated the need for time-consuming adjustments typically required for fitting standard mesh implants, enhancing surgical efficiency. In addition, the size of the cortical bone fenestration was reduced by 20%, compared to the planned reduction of 30%. This deviation occurred due to slight over-removal of cortical bone during tumor curettage, attributed to the thinning of the cortical layer in the affected region. Compared to non-shape memory implants, the use of the 4D implant resulted in smaller fenestrations and preserved more cortical bone. This preservation is particularly beneficial for maintaining the structural integrity and biomechanical stability of the defect site. As a result, after an intraoperative comprehensive evaluation, no additional fixation plate was required. Post-operative imaging confirmed the proper positioning of the implant, and subsequent follow-ups demonstrated satisfactory bone integration, as evidenced by radiographic assessments. The integration of autologous bone grafts within the porous structure facilitated robust osseointegration. Autografts/allografts exhibit good biocompatibility and osteointegration potential but lack sufficient mechanical integrity for structural support in load-bearing defects.[38] In contrast, polymethylmethacrylate bone cements provide immediate mechanical stability; however, they do not integrate with host bone and may act as inert fillers without promoting biological healing.[39] The 4D-printed NiTi scaffold overcomes both limitations by combining anatomical adaptability with a porous structure that supports bone ingrowth, making it well-suited for minimally invasive reconstruction of cavitary bone defects. However, a potential concern with NiTi alloys is the release of nickel ions, which may induce allergic or cytotoxic responses. Nevertheless, prior studies have demonstrated that the ion release from medical-grade NiTi implants remains minimal and well within clinically acceptable limits.[40,41] Furthermore, surface treatments, such as electropolishing and controlled oxidation, can significantly enhance corrosion resistance and reduce nickel ion leaching.[42,43] In this study, no signs of allergic reaction or inflammation were observed during follow-up, indicating that under the present clinical conditions, the risk of nickel ion toxicity was negligible.

This study also has several limitations. First, the results presented are based on a single clinical case, which limits the ability to draw broader conclusions at this stage. Although the outcomes observed in this preliminary investigation were promising, further studies involving a larger patient cohort are necessary to validate these results. Second, the follow-up duration was limited to the short term, and longer-term evaluations are needed to fully assess the durability, integration, and clinical safety of the 4D-printed NiTi implant. Third, although no adverse reactions were observed in the present study, comprehensive biological evaluations should be conducted in future work to further confirm the biosafety of the implant.

5. Conclusions

The 4D-printed shape memory NiTi mesh implant shows promising clinical outcomes in treating cavitary bone defects. The implant's time-responsive shape recovery enables MID and conforms precisely to irregular defect geometries. This work highlights the potential of 4D-printed biomaterials as an innovative solution for challenging bone reconstructions, offering both functional and surgical advantages.

Acknowledgement
We would like to express our sincere gratitude to Engineer Chunchun Chen for her invaluable assistance with the model processing.
Financial support
This work was supported by the Natural Science Foundation of Sichuan Province (2024NSFSC7665, 2023NSFSC1589) and the National Natural Science Foundation of China (82402816).

Conflicts of interest statement

Shanfang Zou and Ruicheng Liu are employees of Tianqi Additive Manufacturing Co., Ltd. However, they were not involved in any activities that could constitute a conflict of interest in relation to this study.

Author contributions

Conceptualization: ZL and ML; *Data curation:* ZL, ML, SZ, RL, HL, YW, and YZ; *Formal analysis:* ZL, ML, SZ, and RL; *Investigation:* ZL and ML; *Methodology:* ZL, ML, SZ, and RL; *Supervision:* YZ, CZ, YL, LM, and CT; *Writing – original draft:* ZL; *Writing – editing and& review:* HL, YW, YZ, YZ, CZ, YL, LM, and CT. All authors reviewed and approved the final version of the manuscript.

Ethics approval and consent to participate

The procedure involving human participants in this study was reviewed and approved by the Ethics Committee of West China Hospital (approval ID: HX202277). Written informed consent was obtained from the patient for the use of clinical data in the publication.

Consent for publication

Written informed consent was obtained from the patient for the use of clinical data in the publication.

Availability of data

The data presented in this study are available on request from the corresponding author.

References

1. Horstmann PF, Hettwer WH, Petersen MM. Treatment of benign and borderline bone tumors with combined curettage and bone defect reconstruction. *J Orthop Surg (Hong Kong).* 2018;26(3):2309499018774929. doi: 10.1177/2309499018774929
2. Zhang Y, Lu M, Min L, *et al.* Three-dimensional-printed porous implant combined with autograft reconstruction for giant cell tumor in proximal tibia. *J Orthop Surg Res.* 2021;16(1):286. doi: 10.1186/s13018-021-02446-x
3. Qu Z, Yue J, Song N, Li S. Innovations in three-dimensional-printed individualized bone prosthesis materials: Revolutionizing orthopedic surgery: A review. *Int J Surg.* 2024;110:6748-6762. doi: 10.1097/JS9.0000000000001842
4. Yang H, Fang H, Wang C, *et al.* 3D printing of customized functional devices for smart biomedical systems. *SmartMat.* 2023;5:e1244. doi: 10.1002/smm2.1244
5. Gong T, Lu M, Wang J, *et al.* Is three-dimension-printed mesh scaffold an alternative to reconstruct cavity bone defects near joints? *Int Orthop.* 2023;47(3):631-639. doi: 10.1007/s00264-022-05684-8
6. Raucci MG, D'Amora U, Ronca A, Ambrosio L. Injectable functional biomaterials for minimally invasive surgery. *Adv Healthc Mater.* 2020;9(13):e2000349. doi: 10.1002/adhm.202000349
7. Ramezani M, Mohd Ripin Z. 4D printing in biomedical engineering: Advancements, challenges, and future directions. *J Funct Biomater.* 2023;14(7):347. doi: 10.3390/jfb14070347
8. Agarwal T, Hann SY, Chiesa I, *et al.* 4D printing in biomedical applications: Emerging trends and technologies. *J Mater Chem B.* 2021;9(37):7608-7632. doi: 10.1039/d1tb01335a
9. Subash A, Kandasubramanian B. 4D printing of shape memory polymers. *Eur Polym J.* 2020;134:109771. doi: 10.1016/j.eurpolymj.2020.109771
10. Zhang J, Yin Z, Ren L, *et al.* Advances in 4D printed shape memory polymers: From 3D printing, smart excitation, and response to applications. *Adv Mater Technol.* 2022;7(9):2101568. doi: 10.1002/admt.202101568
11. Khalid MY, Arif ZU, Noroozi R, Zolfagharian A, Bodaghi M. 4D printing of shape memory polymer composites: A review on fabrication techniques, applications, and future perspectives. *J Manuf Processes.* 2022;81:759-797. doi: 10.1016/j.jmapro.2022.07.035
12. Shiblee MNI, Ahmed K, Kawakami M, Furukawa H. 4D printing of shape-memory hydrogels for soft-robotic functions. *Adv Mater Technol.* 2019;4(8):1900071. doi: 10.1002/admt.201900071
13. Aydin G, Abdullah T, Okay O. 4D printing of self-healing and shape-memory hydrogels sensitive to body temperature. *Eur Polym J.* 2025;223:113651. doi: 10.1016/j.eurpolymj.2024.113651
14. Amadi A, Mohyaldinn M, Ridha S, Ola V. Advancing engineering frontiers with NiTi shape memory alloys: A multifaceted review of properties, fabrication, and application potentials. *J Alloys Compd.* 2023;976:173227. doi: 10.1016/j.jallcom.2023.173227
15. Maroof M, Sujithra R, Tewari RP. Superelastic and shape memory equi-atomic nickel-titanium (Ni-Ti) alloy in dentistry: A systematic review. *Mater Today Commun.* 2022;33:104352. doi: 10.1016/j.mtcomm.2022.104352
16. L'H Y, Rayes F, Warrak A. Regulation, orthopedic, dental, endovascular and other applications of Ti-Ni shape memory alloys. In: *Shape Memory Alloys for Biomedical Applications.* Netherlands: Elsevier; 2009. p. 306-326.
17. Alipour S, Taromian F, Ghomi ER, Zare M, Singh S, Ramakrishna S. Nitinol: From historical milestones to functional properties and biomedical applications. *Proc Inst Mech Eng Part H.* 2022;236(11):1595-1612. doi: 10.1177/09544119221123176
18. Yu Z, Xu Z, Guo Y, *et al.* Study on properties of SLM-NiTi shape memory alloy under the same energy density. *J Mater Res Technol.* 2021;13:241-250. doi: 10.1016/j.jmrt.2021.04.058
19. Yang Y, Zhan JB, Sui JB, *et al.* Functionally graded NiTi alloy with exceptional strain-hardening effect fabricated by SLM method. *Scr Mater.* 2020;188:130-134. doi: 10.1016/j.scriptamat.2020.07.019
20. Mohamed OA, Masood SH, Xu W. Nickel-titanium shape memory alloys made by selective laser melting: A review on process optimisation. *Adv Manuf.* 2022;10(1):24-58. doi: 10.1007/s40436-021-00376-9
21. Safaei K, Abedi H, Nematollahi M, *et al.* Additive manufacturing of NiTi shape memory alloy for biomedical applications: Review of the LPBF process ecosystem. *Jom.* 2021;73:3771-3786. doi: 10.1007/s11837-021-04937-y
22. Sinha A, Kumar Rajak D, Shaik NB, *et al.* A review on 4D printing of nickel-titanium smart alloy processing, the effect of major parameters and their biomedical applications. *Proc Inst Mech Eng Part E.* 2023:09544089231154416. doi: 10.1177/09544089231154416
23. Li Z, Lu M, Lei H, *et al.* Selective laser melting fabrication of body-temperature shape memory NiTi alloy for 4D-printed orthopedic implants. *Virtual Phys Prototyp.* 2024;19(1):e2413181. doi: 10.1080/17452759.2024.2413181
24. Zhao YL, Zhang HR, Zhang JY, Hu YC. Postoperative functional assessment in patients with tumors around the knee treated with endoprosthetic reconstruction: A multicenter retrospective cohort study. *Technol Cancer Res Treat.* 2023;22:15330338231181283. doi: 10.1177/15330338231181283
25. Wen S, Gan J, Li F, Zhou Y, Yan C, Shi Y. Research status and prospect of additive manufactured nickel-titanium shape memory alloys. *Materials.* 2021;14(16):4496. doi: 10.3390/ma14164496
26. Yang L, Ferrucci M, Mertens R, *et al.* An investigation into the effect of gradients on the manufacturing fidelity of triply periodic minimal surface structures with graded density fabricated by selective laser melting. *J Mater Proc Technol.* 2020;275:116367. doi: 10.1016/j.jmatprotec.2019.116367
27. Yang L, Wu S, Yan C, *et al.* Fatigue properties of Ti-6Al-4V Gyroid graded lattice structures fabricated by laser powder bed fusion with lateral loading. *Add Manuf.* 2021;46:102214.

doi: 10.1016/j.addma.2021.102214
28. Zhang W, Li Z, Chai M, Dong P, Wang Y. Selective laser melting of NiTi cardiovascular stents: Processibility, surface quality and mechanical properties. *Opt Laser Technol.* 2025;181:111842. doi: 10.1016/j.optlastec.2024.111842
29. Liu X, Gu D, Yuan L, *et al.* Topological optimisation and laser additive manufacturing of force-direction-sensitive NiTi porous structures with large deformation recovery behaviour. *Virtual Phys Prototyp.* 2024;19(1):e2365860. doi: 10.1080/17452759.2024.2365860
30. Yang X, Yang Q, Shi Y, *et al.* Effect of volume fraction and unit cell size on manufacturability and compressive behaviors of Ni-Ti triply periodic minimal surface lattices. *Add Manuf.* 2022;54:102737. doi: 10.1016/j.addma.2022.102737
31. Wysocki B, Idaszek J, Zdunek J, *et al.* The influence of selective laser melting (SLM) process parameters on *in-vitro* cell response. *Int J Mol Sci.* 2018;19(6):1619. doi: 10.3390/ijms19061619
32. Lu H, Ma H, Cai W, *et al.* Altered phase transformation behaviors and excellent bending shape memory property of NiTi shape memory alloy via selective laser melting. *J Mater Proc Technol.* 2022;303:117546. doi: 10.1016/j.jmatprotec.2022.117546
33. Wang X, Yu J, Liu J, *et al.* Effect of process parameters on the phase transformation behavior and tensile properties of NiTi shape memory alloys fabricated by selective laser melting. *Add Manuf.* 2020;36:101545. doi: 10.1016/j.addma.2020.101545
34. Shi G, Li L, Yu Z, *et al.* The interaction effect of process parameters on the phase transformation behavior and tensile properties in additive manufacturing of Ni-rich NiTi alloy. *J Manuf Processes.* 2022;77:539-550. doi: 10.1016/j.jmapro.2022.03.027
35. Guo W, Sun Z, Yang Y, *et al.* Study on the junction zone of NiTi shape memory alloy produced by selective laser melting via a stripe scanning strategy. *Intermetallics.* 2020;126:106947. doi: 10.1016/j.intermet.2020.106947
36. Qiu Y, Young ML, Nie X. High strain rate compression of martensitic NiTi shape memory alloys. *Shape Mem Superelasticity.* 2015;1:310-318. doi: 10.1007/s11661-016-3857-0
37. Li C, Zhou Z, Zhu Y. A uniaxial constitutive model for NiTi shape memory alloy bars considering the effect of residual strain. *J Intell Mater Syst Struct.* 2019;30(8):1163-1177. doi: 10.1177/1045389X19835932
38. Santoro A, Voto A, Fortino L, *et al.* Bone defect treatment in regenerative medicine: Exploring natural and synthetic bone substitutes. *Int J Mol Sci* 2025;26(7):3085. doi: 10.3390/ijms26073085
39. Seesala VS, Sheikh L, Basu B, Mukherjee S. Mechanical and bioactive properties of PMMA bone cement: A review. *ACS Biomater Sci Eng.* 2024;10(10):5939-5959. doi: 10.1021/acsbiomaterials.4c00779
40. Mlinaric MR, Durgo K, Katic V, Spalj S. Cytotoxicity and oxidative stress induced by nickel and titanium ions from dental alloys on cells of gastrointestinal tract. *Toxicol Appl Pharmacol.* 2019;383:114784. doi: 10.1016/j.taap.2019.114784
41. Eliades T, Pratsinis H, Kletsas D, Eliades G, Makou M. Characterization and cytotoxicity of ions released from stainless steel and nickel-titanium orthodontic alloys. *Am J Orthod Dentofacial Orthop.* 2004;125(1):24-29. doi: 10.1016/j.ajodo.2003.09.009
42. Chu CL, Wang RM, Yin LH, *et al.* Surface treatment of NiTi shape memory alloy by modified advanced oxidation process. *Trans Nonferrous Metals Soc China.* 2009;19(3):575-580. doi: 10.1016/S1003-6326(08)60315-5
43. Chu CL, Guo C, Sheng XB, *et al.* Microstructure, nickel suppression and mechanical characteristics of electropolished and photoelectrocatalytically oxidized biomedical nickel titanium shape memory alloy. *Acta Biomater.* 2009;5(6):2238-2245. doi: 10.1016/j.actbio.2009.01.046

Received: March 2, 2025
Revised: April 6, 2025
Accepted: April 15, 2025
Available online: May 28, 2025